IEEE Access
Multidisciplinary | Rapid Review | Open Access Journal

Received July 23, 2019, accepted August 4, 2019, date of publication August 9, 2019, date of current version August 23, 2019.

Digital Object Identifier 10.1109/ACCESS.2019.2934130

Coordination Control Strategy for Battery-Ultracapacitor Hybrid Energy Storage System in Microgrids With Unbalanced and Nonlinear Loads

YIXIN ZHU[1], (Member, IEEE), QIGAO FAN[1], (Member, IEEE), LIANSONG XIONG[2], (Member, IEEE), GAOFENG ZHANG[1], AND XIN QIAN[1]

[1]College of Internet of Things Engineering, Jiangnan University, Wuxi 214122, China
[2]School of Automation, Nanjing Institute of Technology, Nanjing 211167, China

Corresponding author: Yixin Zhu (zhuyixin1987@163.com)

This work was supported in part by the National Natural Science Foundation of China (NSFC) under Grant 51807079.

ABSTRACT Hybrid energy storage system (HESS) is widely used in microgrids, and its research mainly focuses on energy management, power allocation, topology design and so on. For the power allocation issue, most research only involves the fundamental power allocation within a single HESS. While the allocation of reactive power, negative sequence power and harmonic power, and the coordinated operation of multiple HESS units are rarely be studied. In response to the above situation, this paper proposes a coordination control strategy for the HESS group under the unbalanced load and nonlinear load conditions. The proposed strategy is based on droop control method and can realize interconnection and power sharing for multiple HESS units under weak communication condition. Inside the HESS, the battery (BAT) power conversion system (PCS) works in droop mode, providing energy and only outputting fundamental active power; and the ultracapacitor (UC) PCS works in the compensation mode, analyzing the output power of HESS and providing the reactive, negative sequence and harmonic powers. This strategy can provide better system performance in unbalanced and nonlinear load conditions. It utilizes UC-PCS to deal with the inherent power sharing issues of droop control method, and enhance the transient process. Meanwhile, the stability of microgrid and the service life of the BAT-PCS are increased with the improvement of power quality. Moreover, the HESS adopts a dual inverter structure, which is conducive for the upgrading of existing equipment. Finally, the validity of the proposed strategy is verified by simulation and experimental results.

INDEX TERMS Microgrid, hybrid energy storage system (HESS), power sharing, coordination control, harmonic power.

I. INTRODUCTION

With the increased concerns on environment and cost of energy, more renewable energy sources (RES) such as photovoltaic cells, small wind turbines, and microturbines are integrated into the power grid in the form of distributed generation (DG) units which are normally interfaced to the grid through power electronics converters. To obtain an efficient management of multiple DG units, the microgrid concept was proposed [1], [2]. The microgrid coordinates inner DG units and integrates them as a controllable unit which can be connected to the power grid through a point of common coupling (PCC). A microgrid can operate in either grid-connected mode or islanded mode, thereby increasing the power supply reliability for the end user. But, with the RES penetration increasing, the stability and power quality issues will appear due to its stochastic nature. Thus, it is necessary to use energy storage system (ESS) to increase the RES penetration and insure its stability [3].

The use of ESS integrates constraints such as admissible bandwidth, maximum ratings, power maximum gradient, as well as the number of cycles. If these constraints are not

The associate editor coordinating the review of this article and approving it for publication was Rui Xiong.

respected, it can lead to a dramatic lifetime reduction of the ESS, or in certain cases, to its destruction [4], [5]. The use of hybrid energy storage system (HESS) offers the necessary tradeoff for increasing the lifetime of each ESS, while also increasing the global specific energy and power of the whole system. One typical case is the battery/ultracapacitor HESS, which utilizes the high energy density of the battery and the high power density of the ultracapacitor. The inner battery is used to provide the low-frequency power required for HESS and the ultracapacitor is used to provide the high-frequency power.

At present, research of HESS mainly focuses on energy management, capacity configuration, power allocation and so on. Among them, the main work of energy management is to arrange the HESS charging and discharging time and power according to the RES and load prediction, so as to smooth power fluctuation of RESs, increase the lifetime of ESSs and achieve optimal scheduling of microgrid [6]–[9]. It does not concern the specific operation of HESS on the micro time scale. So, the HESS studies involving ultracapacitor or other storages with small energy density more focus on the real-time power allocation issue. Whether in the AC or DC microgrid, the basic goal of the HESS is to realize battery protection by dynamically decomposing the HESS power requirement and then coordinating the power outputs of the battery and ultracapacitor [10].

The power allocation between battery and ultracapacitor is a key issue in HESS research. In [11]–[13], the power of HESS is divided into high and low frequency components by the low pass filter (LPF). However, the phase lag in LPF may destroy the system stability. Moving average filter is used in [14], [15] to separate the average power and fluctuating power of HESS. An adaptive fuzzy logic method based on energy management strategy for HESS is discussed in [16]. In [17], a multi-mode fuzzy logic based power allocator for HESS is proposed. The model predictive control (MPC) for the HESS is presented in [18]. In [19], [20], the sliding mode control technique is used to control the HESS. However, the control algorithms are complicated to design. It is worth noting that all these methods belong centralized control. In such system, the net power should be accurately measured, and central controller and communication links are required for power references allocation.

Droop control method, which mimics the characteristics of synchronous generator, can realize interconnection and power sharing of converters without communication [21]–[23]. It can be either used in AC or DC microgrids. In order to improve the stability and accuracy of the droop control, the virtual impedance method is often used in combination with it [24]–[26]. The power sharing among ESSs in HESS can also refer to the above two methods, and decentralized control can be realized, which is more attractive [27].

In [28], a decentralized frequency-coordinating virtual impedance method is proposed for dynamic power sharing. But the combination of proportional controller and HPF for ultracapacitor control will lead to an uncontrolled leakage current at steady state. In [29], an extended droop control method to realize power sharing between the battery and ultracapacitor during the load and generation variations is proposed based on virtual resistance and virtual capacitance controllers. Similar technique is used in [30], [31]. However, these methods are only applied in DC microgrid. Then, in [32], a simplified virtual impedance method for parallel-connected 3-phase inverters is proposed to obtain dynamic power sharing between the battery and ultracapacitor in AC microgrid.

From above research, it can be found that, for the power allocation issue of HESS, most research divides power into high and low frequency components. This is feasible for DC microgrids, but for AC microgrids, the power composition is more complex. For example, the fundamental power can be divided into active and reactive powers; negative sequence power and harmonic powers will be contained if unbalanced and nonlinear loads exist in the microgrid. However, only the decomposition of fundamental active power is considered in above research on AC microgrid. On the other hand, there has been research on the power allocation within a single HESS, or the power allocation between HESS and external RESs, but the power allocation among multiple HESSs is rarely considered.

To solve the above issues, in this paper, a power allocation strategy for the HESS group under the unbalanced load and nonlinear load conditions is proposed. The proposed HESS adopts dual inverter structure, including a battery PCS (BAT-PCS) and an ultracapacitor PCS (UC-PCS). In the strategy, the power allocation between the two inner PCSs, and the power sharing among HESSs are both studied. The BAT-PCS, as the main unit in the HESS, adopts the droop control method to ensure active power sharing among HESSs; the UC-PCS, as the auxiliary unit, works in compensation mode, outputting reactive, negative sequence and harmonic powers. During load or generation variations, the UC-PCS will extra provide high-frequency active power to make up for the low power density of the BAT-PCS.

The paper is organized as follows. The microgrid concept and power sharing issue of droop control method are briefly discussed in Section II. The structure and application of the HESS are introduced in Section III, as well as the control strategy. Related parameter design and stability analysis are presented in Section IV. Simulation and experimental results are given in Section V and VI to validate the effectiveness of the proposed control strategy. Conclusions are finally drawn in Section VII.

II. POWER SHARING ISSUE IN DROOP CONTROLLED MICROGRID

A. DROOP CONTROL IN NETWORKED MICROGRID

Figure 1 illustrates the configuration of an AC microgrid composed of DG units such as RES and ESS. These DG units can be connected to any node of the network. Loads connected directly to the DG units are called local loads,

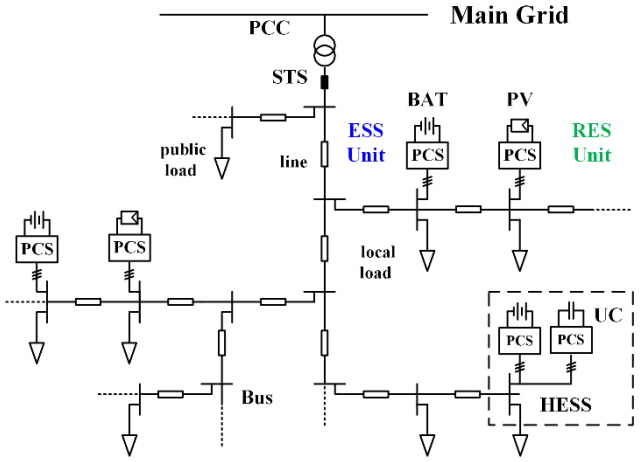

FIGURE 1. Illustration of the networked microgrid.

and the others are public loads. By controlling the static transfer switch (STS) at the PCC, the microgrid can operate in either islanded mode or grid-connected mode. In the grid-connected mode, voltage of the microgrid is supported by the main grid, so the power sharing issue can be easily solved by adopting power tracking techniques. However, in the islanded mode, the ESSs need to solve the dual problem of voltage support and power sharing. The total power demand of ESSs is determined by the RESs and loads. It should be properly shared among multiple RESs according to the power rating and state of charge (SOC).

To solve the power sharing issue in islanded microgrid, the conventional droop control method is usually applied to the BAT-PCS, and its control expressions are as follows:

$$f^* = f_0 - D_p P \tag{1}$$

$$E^* = E_0 - D_q Q \tag{2}$$

where f_0 and E_0 are the initial value of the frequency and voltage magnitude of the DG unit, respectively; P and Q are the measured active and reactive powers after the first-order low-pass filtering (LPF), respectively; D_p and D_q are the active and reactive power droop slopes, respectively. When SOC is not considered, they are normally associated with the power rating of the DG unit, which can be defined as

$$D_p = \frac{f_{max} - f_{min}}{P_{max}} \tag{3}$$

$$D_q = \frac{E_{max} - E_{min}}{Q_{max}} \tag{4}$$

where f_{max} and f_{min} are the upper and lower bounds of the microgrid frequency, respectively; E_{max} and E_{min} are the upper and lower bounds of the microgrid voltage, respectively; P_{max} and Q_{max} are the active and reactive power ratings of the DG unit. With the derived frequency and voltage magnitude, the instantaneous voltage reference of the DG unit can be obtained accordingly. According to (3) and (4), the droop slopes are inversely proportional to the DG capacities. Thus, the DG unit with larger capacity will be

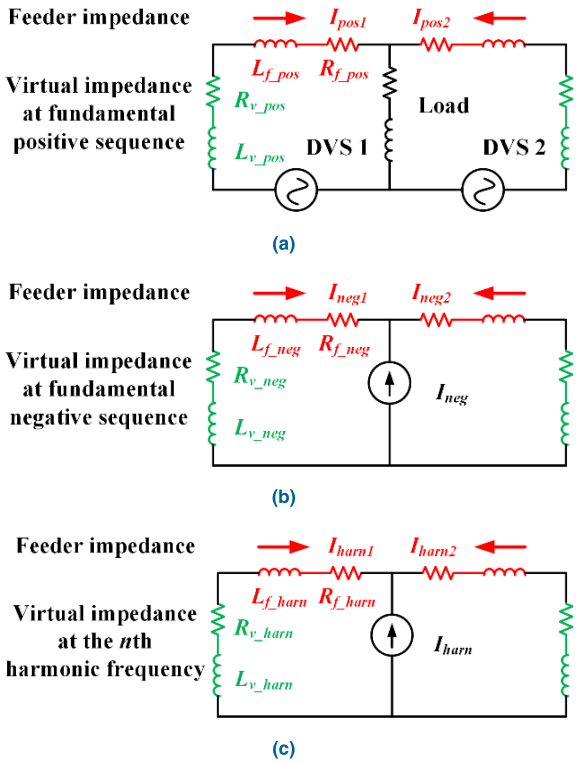

FIGURE 2. Equivalent circuits of a parallel system at different frequencies and sequences. (a) Equivalent circuit at fundamental positive sequence. (b) Equivalent circuit at fundamental negative sequence. (c) Equivalent circuit at harmonic frequencies.

set with smaller droop slopes, and vice versa. So that when all the DG units operate under the same frequency and voltage magnitude, the larger capacity DG units can output more real and reactive powers according to (1) and (2). And this is the power sharing principle of droop control. Although the DG units have the same frequency, the voltage magnitudes of DG units can hardly be unified due to the mismatch in network parameters [33]. So, the Q-V droop control always suffers reactive power sharing issues.

B. POWER SHARING ISSUES

To reveal the causes of the reactive power sharing issue in droop control, a parallel system composed of two same droop-controlled DG units is introduced, with the equivalent circuit sketched in Figure 2. The equivalent circuit at fundamental positive sequence is presented in Figure 2(a). As the figure shows, the DG unit is equivalent to a droop-controlled voltage source (DVS), meanwhile the virtual impedance is added to maintain the system stable.

Assume the virtual impedances of the two DG units are the same, but due to the differences in physical feeder impedances, the two DVSs will have different port voltages. According to (2), the reactive power outputs of the two DVSs will also be different, and thus resulting in reactive power sharing errors. This is the main cause of reactive power sharing issue. If the virtual impedance values are well set,

the mismatch in physical feeders can be compensated, eliminating the reactive power sharing errors. If unbalanced load is connected between the two DG units, negative sequence current will be generated.

The equivalent circuit at fundamental negative sequence is presented in Figure 2(b), where the unbalanced central load is described as a current source I_{neg}. Due to the differences in the feeder impedances of the two sides, the two DG units will be distributed different negative sequence powers. If nonlinear load is in the center, harmonic current will be generated. The equivalent circuit at a given harmonic frequency is given in Figure 2(c), and the situation of harmonic power sharing is similar to that of unbalanced power. But the actual microgrid system is much more complex than the parallel system shown in Figure 2, the mismatch among DG units is not only caused by the feeder impedances but also by the local load and location of DG units, making power sharing issues more complicated. Moreover, the negative sequence and harmonic powers will lead to the poor performance of DG units.

C. POWER SHARING RESEARCHE

At the beginning, the microgrid structure is simple, which contains a common AC bus. All the DG units are connected to it through their own feeders. The system structure is regular, and by adding virtual impedance to DG units, the mismatched line parameters can be offset, and accurate power sharing performance can be achieved [34]–[36]. However, when the microgrid structure is networked as Figure 1 shows, these non-communication solutions cannot provide satisfactory reactive power sharing performance.

To solve the reactive power sharing issue of droop control in networked microgrids, communication is commonly used. Synchronizing signals are utilized in [37] to trigger an extra regulation process for reactive power sharing, but the control performance is easy to be influenced if load changes during the regulation period. By establishing communication links between the microgrid central controller (MGCC) and DG units, reactive power sharing can be achieved through the centralized control [38], [39]. In recent years, decentralized control methods based on the multi-agent consensus protocol are developed, which can provide accurate power sharing performance by only using a sparse communication network [40], [41]. Differ from the centralized control, DG units only communicate with their neighbor units in this control. In [33] and [42], a non-communication method is proposed for the power sharing in networked microgrid. However, the method requires detailed network parameters, limiting its application. With the help of communication, the negative sequence and harmonic power sharing issues can also be solved. Based on the above-mentioned centralized control, virtual impedances at negative-sequence and harmonic frequencies are developed to realize negative sequence and harmonic power sharing [43], [44]. Then, the consensus protocol based harmonic power sharing method is proposed in [45].

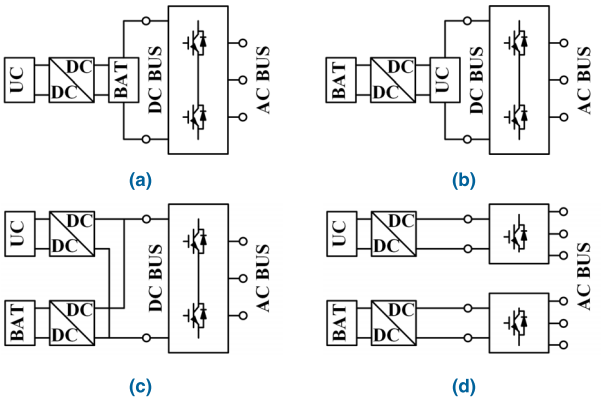

FIGURE 3. HESS topologies used in the microgrid. (a) UC-only connected through a dc/dc converter. (b) BAT-only connected through a dc/dc converter. (c) BAT/UC connected through the respective dc/dc converters. (d) BAT/UC connected through the respective inverters.

From above research, it can be found that communication is an essential measure for the power sharing of DG units in networked microgrid. However, it will affect the ''plug and play'' feature of the DG unit. In this paper, by effectively using the UC-PCS, this problem can be solved.

III. CONTROL STRATEGY OF THE PROPOSED HESS

A. HESS TOPOLOGIES SELECTION FOR POWER SHARING

As mentioned above, in non-communication condition, the droop control can only realize active power sharing with the help of the frequency relation among DG units. If the HESS is well designed, the power sharing among BAT-PCSs can be realized without communication.

Figure 3 shows the main structures currently found in the literature to integrate a HESS into a microgrid.

In these topologies, the first three topologies combine ESSs at the DC side. These topologies have their own advantages, but it is difficult for them to solve the power sharing issue at the AC side. Since this paper studies the AC power allocation issue under unbalanced and nonlinear load conditions, the topology shown in Figure 3(d) is selected.

The simple structure of the proposed HESS is illustrated in Figure 1, which can be regarded as a parallel system composed of a BAT-PCS and an UC-PCS. In this HESS, the BAT-PCS works as the traditional DG unit, while the UC-PCS is used to provide the high frequency active power in transient state for the BAT-PCS. It also provides reactive, negative sequence and harmonic powers in steady state to enhance the power quality of the BAT-PCS. The main circuit of the HESS is shown in Figure 4. The BAT-PCS and UC-PCS have their respective control chips, and the frequency of the BAT-PCS is sent to UC-PCS through local communication link. The two PCSs have a similar structure: the first stage is a bidirectional buck-boost converter, and the second stage is a three-phase half-bridge inverter. In discharge state, the energy flows from the first stage to the second stage, and the bidirectional buck-boost converter works in boost mode. While in charge state, the energy flows from the second stage

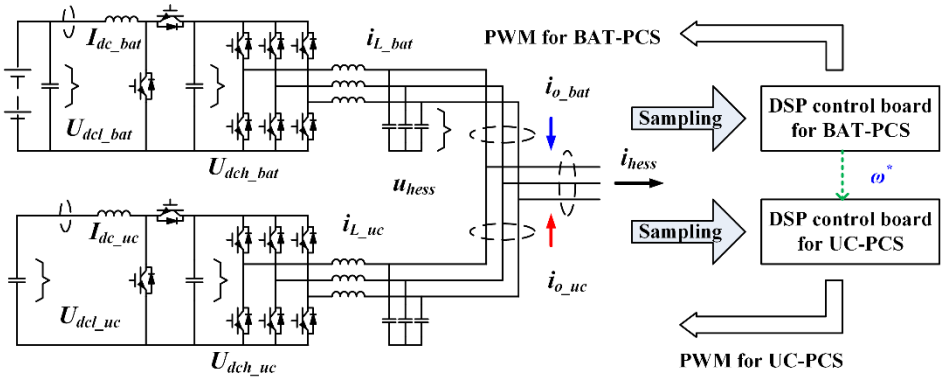

FIGURE 4. Main circuit of the proposed HESS.

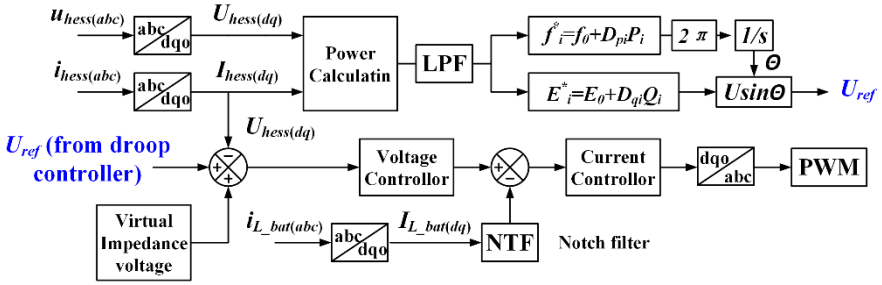

FIGURE 5. Control diagram of the BAT-PCS.

to the first stage, and the bidirectional buck-boost converter works in buck mode.

B. INTERNAL CONTROL STRATEGY OF THE HESS

By applying the droop control method to the BAT-PCS, the proposed HESS can operate in parallel. The control diagram of the BAT-PCS with the droop control method is shown in Figure 4.

As can be seen from the figure, the BAT-PCS only uses the traditional droop control method. When D_p and D_q equal zero, the battery PCS will turn to VF mode, outputting constant voltage and frequency. In addition, when integral controllers are added to D_p and D_q, the BAT-PCS will turn to PQ mode, outputting the specified active and reactive power. If UC-PCSs are not considered, loads in microgrid will be shared by the parallel BAT-PCSs. As mentioned before, reactive power sharing errors will appear in the system. If unbalanced load and harmonic loads are contained in the system, there will also be negative sequence and harmonic power sharing errors. To realize accurate power sharing among BAT-PCSs, the UC-PCS is used here, which works as an auxiliary unit of the BAT-PCS. The output current of the HESS $\boldsymbol{i_{hess}}$ is actually the BAT-PCS current before the UC-PCS introduced, and it is now composed of the BAT-PCS current $\boldsymbol{i_{o\_bat}}$ and UC-PCS current $\boldsymbol{i_{o\_uc}}$. According to the respective characteristics of the BAT-PCS and UC-PCS, they will take charge of outputting different currents. For better illustration, suppose the voltage and current expressions of the HESS are as follows (5), as shown at the bottom of the next page, where, U_{hess} is the voltage magnitude of the HESS; I_1^+ and I_1^- are the magnitudes of the fundamental positive sequence and negative sequence currents, respectively; I_5^-, I_7^+, I_{11}^- and I_{13}^+ are the magnitudes of the 5th, 7th, 11th and 13th harmonic currents, respectively. The respective current components of the BAT-PCS and UC-PCS are shown in Table 1.

In the table, $\boldsymbol{i_{1d}^+}$ and $\boldsymbol{i_{1q}^-}$ are active and reactive components the fundamental positive sequence current, respectively. Their expressions are as follows:

$$\boldsymbol{i_{1d}^+} = I_1^+ cos\left(\varphi_1^+\right) \begin{bmatrix} sin\left(\omega t\right) \\ sin\left(\omega t - \frac{2}{3}\pi\right) \\ sin\left(\omega t + \frac{2}{3}\pi\right) \end{bmatrix} \tag{7}$$

$$\boldsymbol{i_{1q}^+} = I_1^+ sin\left(\varphi_1^+\right) \begin{bmatrix} cos\left(\omega t\right) \\ cos\left(\omega t - \frac{2}{3}\pi\right) \\ cos\left(\omega t + \frac{2}{3}\pi\right) \end{bmatrix} \tag{8}$$

In steady state, there is no high frequency component in $\boldsymbol{i_{1d}^+}$, all the demanded active current will be outputted by the BAT-PCS. Although the UC-PCS outputs the compensate current, there is no energy consumption in the ultracapacitor. While in transient state, the high frequency component

TABLE 1. Different current components outputted by the BAT-PCS and UC-PCS.

	Fundamental current	Harmonic current
BAT-PCS	i^+_{1d}(low frequency)	—
UC-PCS	i^+_{1d}(high frequency)	i^+_5
	i^+_{1q}	i^+_7
	i^-_1	i^-_{11}
		i^+_{13}

in i^+_{1d} will be provided by the UC-PCS, and this process will consume some energy. When the ultracapacitor SOC reaches its lower bound, the UC-PCS will turn to charged mode. Comparing with the discharge frequency, the charge frequency is much lower.

C. EXTERNAL CONTROL STRATEGY OF THE HESS

The power allocation strategy in the single HESS has been introduced above. When the microgrid contains several such HESSs, they need cooperate together to maintain the voltage and frequency of the microgrid and also share the load demand. So, the networking strategy is required. To adapt different requirements, the HESS is designed to have several external coordination strategies, as listed in Table 2. The HESS can operate in either master and slave mode or peer to peer mode. In master and slave mode, one HESS with large capacity is set as the master unit, working in VF mode. The others work in PQ mode. In peer to peer mode, all the HESSs work in Droop mode and support the microgrid voltage together.

D. CONTROL STRATEGY OF THE UC-PCS

The current of the HESS may contain fundamental positive, negative sequence and harmonic components according to the load, while the BAT-PCS only outputs the fundamental active current i^+_{1d} due to the compensation effect of the UC-PCS.

TABLE 2. Different networking strategies of the HESS.

Networking strategy	PCS	Islanded	Grid-connected
Master-slave mode	BAT-PCS	VF or PQ mode	PQ mode
	UC-PCS	**compensation mode**	**compensation mode**
Peer to peer mode	BAT-PCS	Droop mode	Droop mode
	UC-PCS	**compensation mode**	**compensation mode**

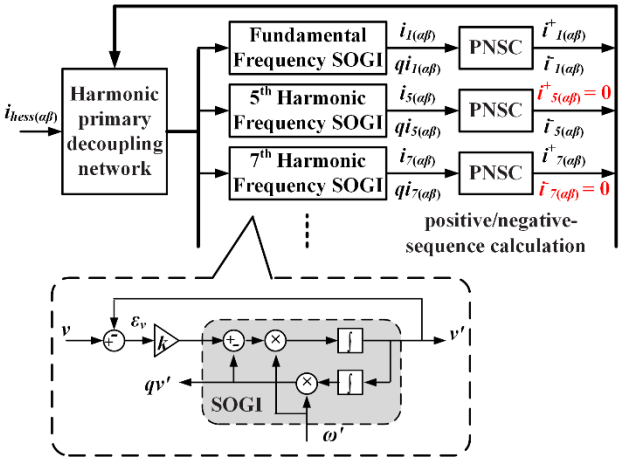

FIGURE 6. Decomposition of the fundamental positive sequence, fundamental negative sequence, and harmonic currents.

The UC-PCS detects the HESS port current and abstracts the required current components to constitute its reference current. Its function is similar to the active power filter (APF), but can provide active power during power fluctuations. By using the second-order generalized integrator (SOGI) method in [20], the fundamental and harmonic currents can be separated. The simplified detection diagram is sketched in Figure 6.

$$\boldsymbol{u_o}=\begin{bmatrix}u_a\\u_b\\u_c\end{bmatrix}=U_{hess}\begin{bmatrix}\sin(\omega t)\\ \sin\left(\omega t-\frac{2}{3}\pi\right)\\ \sin\left(\omega t+\frac{2}{3}\pi\right)\end{bmatrix},\quad \boldsymbol{i_{hess}}=\begin{bmatrix}i_a\\i_b\\i_c\end{bmatrix}=\boldsymbol{i^+_1}+\boldsymbol{i^-_1}+\boldsymbol{i^-_5}+\boldsymbol{i^+_7}+\boldsymbol{i^-_{11}}+\boldsymbol{i^+_{13}}+\ldots \tag{5}$$

$$\begin{aligned}
\boldsymbol{i^+_1}&=I^+_1\begin{bmatrix}\sin\left(\omega t+\varphi^+_1\right)\\ \sin\left(\omega t-\frac{2}{3}\pi+\varphi^+_1\right)\\ \sin\left(\omega t+\frac{2}{3}\pi+\varphi^+_1\right)\end{bmatrix},\quad \boldsymbol{i^+_7}=I^+_7\begin{bmatrix}\sin\left(7\omega t+\varphi^+_7\right)\\ \sin\left(7\omega t-\frac{2}{3}\pi+\varphi^+_7\right)\\ \sin\left(7\omega t+\frac{2}{3}\pi+\varphi^+_7\right)\end{bmatrix},\quad \boldsymbol{i^+_{13}}=I^+_{13}\begin{bmatrix}\sin\left(13\omega t+\varphi^+_{13}\right)\\ \sin\left(13\omega t-\frac{2}{3}\pi+\varphi^+_{13}\right)\\ \sin\left(13\omega t+\frac{2}{3}\pi+\varphi^+_{13}\right)\end{bmatrix},\ldots\\
\boldsymbol{i^-_1}&=I^-_1\begin{bmatrix}\sin\left(\omega t+\varphi^-_1\right)\\ \sin\left(\omega t+\frac{2}{3}\pi+\varphi^-_1\right)\\ \sin\left(\omega t-\frac{2}{3}\pi+\varphi^-_1\right)\end{bmatrix},\quad \boldsymbol{i^-_5}=I^-_5\begin{bmatrix}\sin\left(5\omega t+\varphi^-_5\right)\\ \sin\left(5\omega t+\frac{2}{3}\pi+\varphi^-_5\right)\\ \sin\left(5\omega t-\frac{2}{3}\pi+\varphi^-_5\right)\end{bmatrix},\quad \boldsymbol{i^-_{11}}=I^-_{11}\begin{bmatrix}\sin\left(11\omega t+\varphi^-_{11}\right)\\ \sin\left(11\omega t+\frac{2}{3}\pi+\varphi^-_{11}\right)\\ \sin\left(11\omega t-\frac{2}{3}\pi+\varphi^-_{11}\right)\end{bmatrix}\ldots
\end{aligned} \tag{6}$$

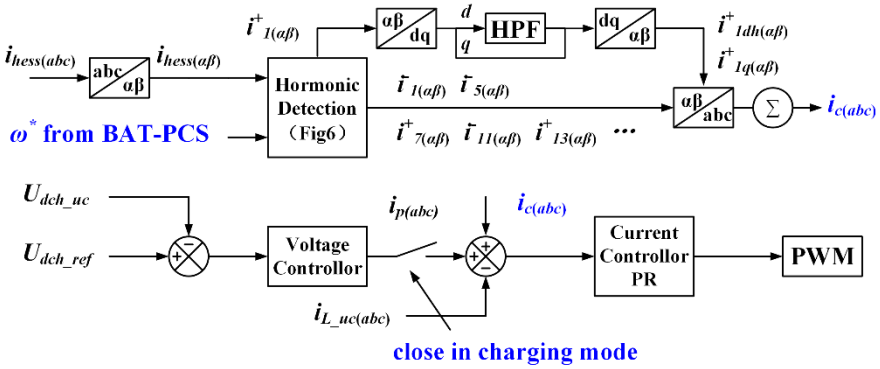

FIGURE 7. Control diagram of the UC-PCS.

Firstly, the 3-phase currents are transferred into the α and β two phases. Then, through the filtering function of the SOGI block, the specific harmonic currents are extracted. Finally, the detected currents are sent to the positive/negative sequence calculation (PNSC) block to further separate the positive and negative sequence components. The transformations in PNSC are as follows:

$$\boldsymbol{v}^+_{\alpha\beta} = \frac{1}{2}\begin{bmatrix} 1 & -q \\ q & 1 \end{bmatrix} \boldsymbol{v}_{\alpha\beta} \tag{9}$$

$$\mathbf{v}^-_{\alpha\beta} = \frac{1}{2}\begin{bmatrix} 1 & q \\ -q & 1 \end{bmatrix} \boldsymbol{v}_{\alpha\beta} \tag{10}$$

where

$$\boldsymbol{v}_{\alpha\beta} = \sqrt{\frac{2}{3}}\begin{bmatrix} 1 & -\frac{1}{2} & -\frac{1}{2} \\ 0 & \frac{\sqrt{3}}{2} & -\frac{\sqrt{3}}{2} \end{bmatrix} \boldsymbol{v}_{abc}$$

$$q = e^{-j(\pi/2)}$$

and q is a 90° -lagging phase-shifting operator applied on the time domain to obtain an in-quadrature version of the input waveforms. In the detected currents, besides the fundamental active current $\boldsymbol{i}^+_{1\boldsymbol{d}}$, all the other currents will be combined to constitute the reference current of the UC-PCS. More details of the harmonic detection algorithm can be found in [46].

The complete control diagram of the control strategy of the UC-PCS is sketched in Figure 7. As mentioned before, the rotating coordinate system of the UC-PCS keeps synchronized with that of the BAT-PCS, and they share the frequency information. Comparing with the common APF, the software phase lock loop (SPLL) block is not needed in UC-PCS, it can realize quicker and more accurate harmonic detection.

During the discharging mode, the DC voltage U_{dch_uc} is supported by the bidirectional buck-boost converter. While in the charging mode, to maintain U_{dch_uc} constant, the outer DC voltage closed-loop control is utilized, which generates the active current reference $\boldsymbol{i}_{p(abc)}$ for the later current closed-loop. To better track the compensation current reference $\boldsymbol{i}_{c(abc)}$, the proportional-resonant (PR) controller is used, and the control expression is as follows

$$G_{PR}(s) = K_P + \sum\nolimits_{h=1,5,7\ldots} \frac{2k_{ih}\omega_b s}{s^2 + 2\omega_b s + (h\omega^*)^2} \tag{11}$$

where k_{ih} is the gain of the resonant controllers in the inner current control loop; ω_b is the bandwidth of the resonant controllers, and k_P is the gain of the proportional control. The angular frequency ω^* is provided by the BAT-PCS. With the proposed current compensation control method, the UC-PCS will output the fundamental positive sequence reactive current, fundamental negative sequence current and harmonic current for the external network. And the BAT-PCS only outputs the fundamental positive sequence active current $\boldsymbol{i}^+_{\boldsymbol{1d}}$. Since there is no negative sequence component and harmonic component in the current of the BAT-PCS, it can output ideal symmetric sinusoidal voltage for the microgrid. In brief, due to the assist role of the UC-PCS, the BAT-PCS can operate in a favorable state and improve the voltage quality of the microgrid.

IV. STABILITY ANALYSIS

Based on the control diagram shown in Figure 7, Figure 8 gives the s-domain model of the UC-PCS with the current compensation control method in the stationary frame. $G_{\mathrm{H}}(s)$ is the harmonic detection block; $G_{\mathrm{i}}(s)$ is the current PR controller; K_{PWM} is the gain of the PWM inverter, which equals $0.5U_{dch\_uc}$; $G_{\mathrm{d}}(s)$ is the computation delay of one sampling period, which can be expressed as

$$G_d(s) = e^{-T_d s} \approx \frac{1}{1 + T_d s} \tag{12}$$

The design of the current controller is based on the dynamic operation requirements. It should realize current tracking as fast as possible under the premise of stability. According to Figure 8, the transfer function of the current control loop can be derived as

$$G_o(s) = G_{io}(s)\, i_c(s) + G_{uo}(s)\, u_{hess}(s) \tag{13}$$

where, $G_{io}(s)$ is the transfer function from the compensation current reference $i_c(s)$ to the UC-PCS output current $i_{o\_uc}(s)$; and $G_{uo}(s)$ is the transfer function from the external

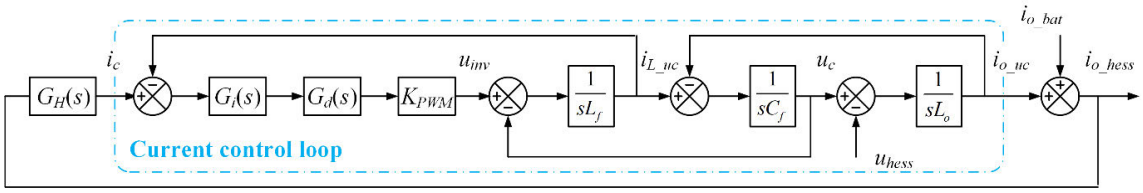

FIGURE 8. Model of the UC-PCS with the current compensation control method.

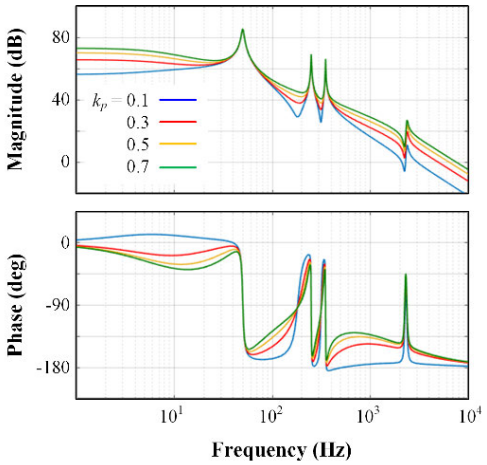

FIGURE 9. Open-loop bode diagrams of the current loop under different k_P values.

voltage $u_{hess}(s)$ to the output current. The detailed expression of $G_{io}(s)$ and $G_{uo}(s)$ are shown at the bottom of the next page. The open loop transfer function from $i_c(s)$ to $i_{o\_uc}(s)$ is given in (16), as shown at the bottom of the next page. Next, by observing the variations of the bode diagram under different parameters, the PR controller will be designed.

1) PROPORTIONAL GAIN

Figure 9 depicts the bode diagrams of the current loop with different k_P values, and the other related control and circuit parameters are listed in Table 3.

Due to the PR controller, the system has high gain at the selected frequency, which increases the accuracy of current tracking. The proportional gain k_P is tuned the same way as for a P controller, and it determines the crossover frequency of the control system. With the decrease of the gain k_P, the crossover frequency will fall, and the anti-high-frequency interference ability will increase. Normally, the crossover frequency is designed between 1/6 and 1/4 of the switching frequency.

When $k_P = 0.1$, the crossover frequency is about 2 kHz. But the stability of the system is poor as can be seen from the phase-frequency characteristic. The selection of k_P is a trade-off between the anti-high-frequency interference and stability. Finally, k_P is set as 0.3 in the simulation system.

2) BANDWIDTH OF THE RESONANT CONTROLLER

Figure 10 depicts the bode diagrams of the current loop with different ω_b values.

TABLE 3. Different networking strategies of the HESS.

Circuit Parameters		**Values**
Feeder Line	Feeder 1	$R_{f1} = 0.06\ \Omega$, $L_{f1} = 0.025$ mH
	Feeder 2	$R_{f2} = 0.06\ \Omega$, $L_{f2} = 0.025$ mH
	Feeder 3	$R_{f3} = 0.12\ \Omega$, $L_{f3} = 0.050$ mH
	Feeder 4	$R_{f4} = 0.06\ \Omega$, $L_{f4} = 0.025$ mH
BAT PCS	LC Filter	$L_f = 1.5$ mH, $C_f = 100$ μF
	Frequency	$f_s = 10$ kHz
UC PCS	LC Filter	$L_f = 1$ mH, $C_f = 50$ μF, $L_o = 0.13$ mH
	Frequency	$f_s = 10$ kHz
Control Parameters		**Values**
BAT PCS	Droop Slopes	$D_p = 8 \times 10^{-6}$, $D_q = 8 \times 10^{-5}$
	Initial Voltage	$E_0 = 320$ V, $F_0 = 50.24$ Hz
	Voltage Controller	$k_{PV} = 10$, $k_{IV} = 100$
	Current Controller	$k_{PI} = 0.1$, $k_{II} = 10$
UC PCS	Voltage Controller	$k_{PV} = 3.2$, $k_{IV} = 0.3$
	Current Controller	$k_P = 0.3$, $k_{1h} = 20$, $k_{5h} = k_{7h} = 16$
Load Condition		**Values**
Case 1	Three-phase balanced Load	$P_{L1} = 30$ kW, $Q_{L1} = 30$ kVar, $P_{L2} = 45$ kW, $Q_{L2} = 45$ kVar
Case 2	Imbalanced Load	Remove the load in phase C
Case 3	Three-phase Diode Rectifier	$R_{d1} = R_{d2} = 8\ \Omega$, $C_{d1} = C_{d2} = 5$ μF

The ω_b determines the width of the resonant peak. It can be selected according to the frequency variation range of the microgrid. Too narrow ω_b may cause the resonant peak drift when the grid frequency varies too much. In the simulation, the bandwidth ω_b is set as 8.

3) GAIN OF THE RESONANT CONTROLLER

Figure 11 depicts the bode diagrams of the current loop with different k_{ih} values. k_{ih} at high frequencies should not be too large to prevent degradation of the phase margin. Finally, the $k_{ih}$is set as follows, $k_{1h} = 20$, $k_{5h} = 16$ and $k_{7h} = 16$. The 11th and 13th resonant gain can be designed in a similar way.

V. SIMULATION RESULTS

A microgrid model is established in Matlab/Simulink to validate the proposed coordination control strategy. As shown in Figure 12, the simulated microgrid is composed of three

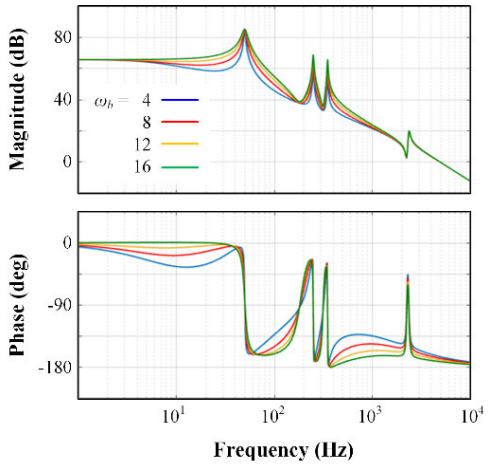

FIGURE 10. Open-loop bode diagrams of the current loop under different ω_b values.

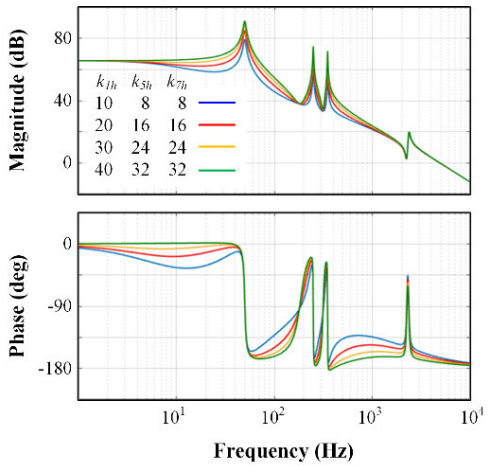

FIGURE 11. Open-loop bode diagrams of the current loop under different k_{ih} values.

identical HESSs and several loads. With the same power rating, the three inner BAT-PCSs should share the load equally. As the control strategy is totally distributed, there is no communication link among these HESSs. The parameters of the HESS and microgrid network, as well as the load conditions are listed in Table 3.

A. CASE 1: BALANCED LOAD

1) PERFORMANCE OF TRADITIONAL STRATEGY

In this simulation case, Load 1 and Load 2 are both 3-phase balanced loads, and the HESSs use the traditional

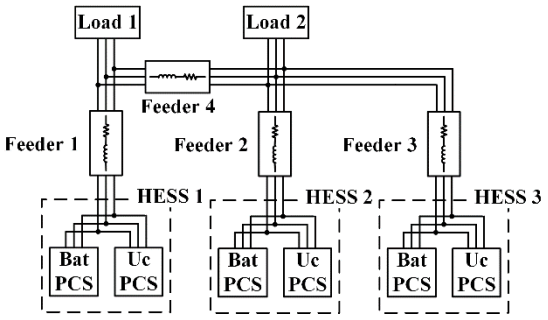

FIGURE 12. Structure of the simulated microgrid.

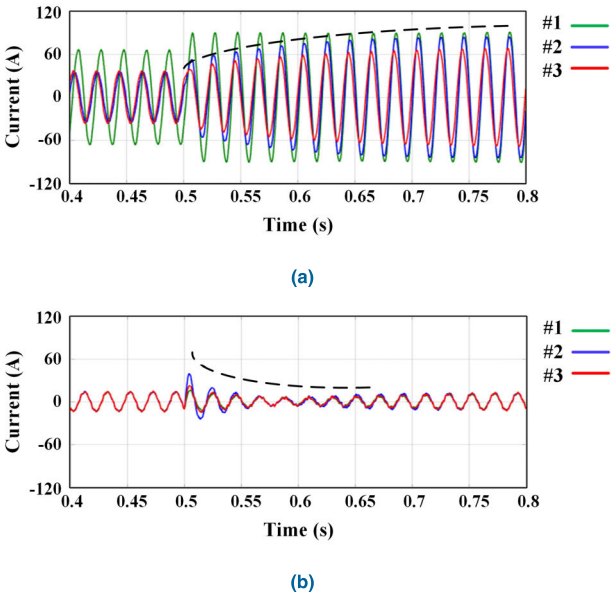

FIGURE 13. Simulated currents obtained in Case 1 with the traditional strategy. (a) Phase A currents of the three BAT-PCSs. (b) Phase A currents of the three UC-PCSs.

coordination control strategy, in which the UC-PCS only compensates the high frequency active current. At the beginning, only Load 1 is connected. According to the characteristics of the droop control, the three BAT-PCSs output the same active current but different reactive current. The simulated currents of the BAT-PCSs and UC-PCSs are shown in Figure 13. It can be seen that the output current of each BAT-PCS is different in magnitude and phase. Meanwhile, the UC-PCSs are under dormant state and there are a few

$$G_{io}(s) = \frac{\left(1 + R_c C_f s\right) G_i(s) G_d(s) K_{PWM}}{\left(L_f s + R_L\right)\left(C_f L_o s^2 + 1 + R_c C_f s\right) + \left(1 + R_c C_f s\right) L_o s + \left(C_f L_o s^2 + 1 + R_c C_f s\right) G_i(s) G_d(s) K_{PWM}} \tag{14}$$

$$G_{uo}(s) = -\frac{s C_f G_i(s) G_d(s) K_{PWM} + \left(L_f s + R_L\right) C_f s + R_c C_f s + 1}{\left(C_f L_o s^2 + 1 + R_c C_f s\right) G_i(s) G_d(s) K_{PWM} + \left(L_f s + R_L\right)\left(C_f L_o s^2 + 1 + R_c C_f s\right) + \left(1 + R_c C_f s\right) L_o s} \tag{15}$$

$$G_{io\_open}(s) = \frac{\left(C_f L_o s^2 + 1 + R_c C_f s\right) G_i(s) G_d(s) K_{PWM}}{L_f C_f L_o s^3 + L_f R_c C_f s^2 + L_o R_c C_f s^2 + R_L C_f L_o s^2 + L_f s + R_L R_c C_f s + L_o s + R_L} \tag{16}$$

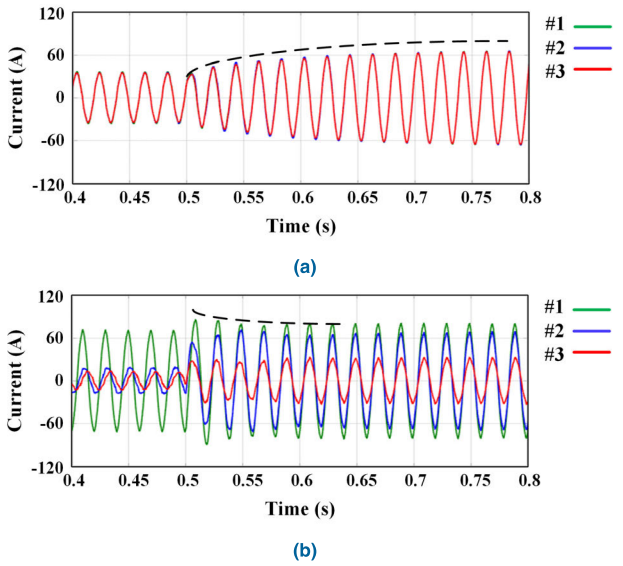

FIGURE 14. Simulated currents obtained in Case 1 with the proposed strategy. (a) Phase A currents of the three BAT-PCSs. (b) Phase A currents of the three UC-PCSs.

reactive currents flowing through the LC filters. When Load 2 connects in at $t = 0.5$ s, due to the compensation role of the UC-PCS, the current of the BAT-PCS should vary gradually as indicated by the dashed line. However, as only the high frequency active current is compensated, and the reactive current is ignored, the currents of the BAT-PCSs still change rapidly. On the other hand, in the whole simulation process, the power sharing of BAT-PCSs has not been realized.

2) PERFORMANCE OF PROPOSED STRATEGY

The performance of system with the proposed coordination control strategy is shown in Figure 14. Comparing with Figure 13, the UC-PCS not only outputs high frequency active current during the load variation, but also output reactive current all the time. As can be seen from Figure 14, the output currents of BAT-PCSs are all the same under the proposed control. The previous reactive currents are outputted by the UC-PCSs.

The high frequency current compensation function of the UC-PCS can also be observed after the load variation. Due to the reactive current compensation role of the UC-PCS, the BAT-PCS currents vary gradually, and the transient process is smoother. Comparing with traditional strategy, the proposed strategy enhances the dynamic performance and realizes the power sharing among BAT-PCSs at the same time.

B. CASE 2: UNBALANCED LOAD

1) PERFORMANCE OF TRADITIONAL STRATEGY

In this case, Load 1 and Load 2 are both unbalanced loads, which do not have load in phase C. The currents of the BAT-PCSs during load variation are illustrated in Figure 15. Due to the phase loss, the 3-phase currents are imbalanced. In ideal condition, the currents of each BAT-PCS should be equal and symmetric. However, there is significant circulation current in the system. The BAT-PCS currents in phase C are not zero. After load varies at $t = 0.5$ s, as the UC-PCS only outputs high frequency active current, the transient performance is not as expected. The compensation effect of UC-PCS is no longer significant as most current is in negative sequence.

2) PERFORMANCE OF PROPOSED STRATEGY

The performance of the system using the proposed strategy is shown in Figure 16. The previous fundamental negative sequence current and reactive current of the BAT-PCS are transferred to the UC-PCS, making the BAT-PCS output the same and symmetric currents. Thus, the power sharing among BAT-PCSs is realized. The outputted compensation currents of the UC-PCSs are shown in Figure 16(b). In the transient process, the UC-PCSs can output both high frequency active current and fundamental negative sequence current, making the BAT-PCS currents vary smoothly.

C. CASE 3: NONLINEAR LOAD

1) PERFORMANCE OF TRADITIONAL STRATEGY

In this case, two 3-phase diode rectifiers are introduced to replace the previous loads. The currents of the BAT-PCSs and UC-PCSs under the traditional control strategy are illustrated in Figure 17. The currents of the BAT-PCSs are nonlinear and unequal, which contains much harmonics. This will affect the voltage quality of the BAT-PCS and further the microgrid.

When load varies at $t = 0.5$ s, the UC-PCSs begin to output high frequency active current. As the harmonic and reactive currents haven't been compensated, the transient process has a poor performance.

2) PERFORMANCE OF PROPOSED STRATEGY

The corresponding system performance of the proposed control strategy is shown in Figure 18. The UC-PCS outputs harmonic current and reactive current for the BAT-PCS, and the latter only outputs the identical active currents due to the frequency regulation role of the droop control. Similar with the above two cases, due to the extra current compensation control of the UC-PCS, the working state of the BAT-PCS is more ideal.

From the above simulation results, it can be seen that the current components are complex in unbalanced and harmonic load conditions, but the traditional strategy only deals with the fundamental positive sequence active current, leading to the poor transient performance. Comparison results shows that the proposed strategy can better deal with the power allocation issue and realize power sharing among BAT-PCSs.

VI. EXPERIMENTAL RESULTS

Experiments are performed to validate the effectiveness of the proposed coordination strategy. A test microgrid system is established in laboratory with 4 inverters as shown in Figure 19. The inverters 1 and 3 which imitate the operation of the BAT-PCS apply the droop control; while the

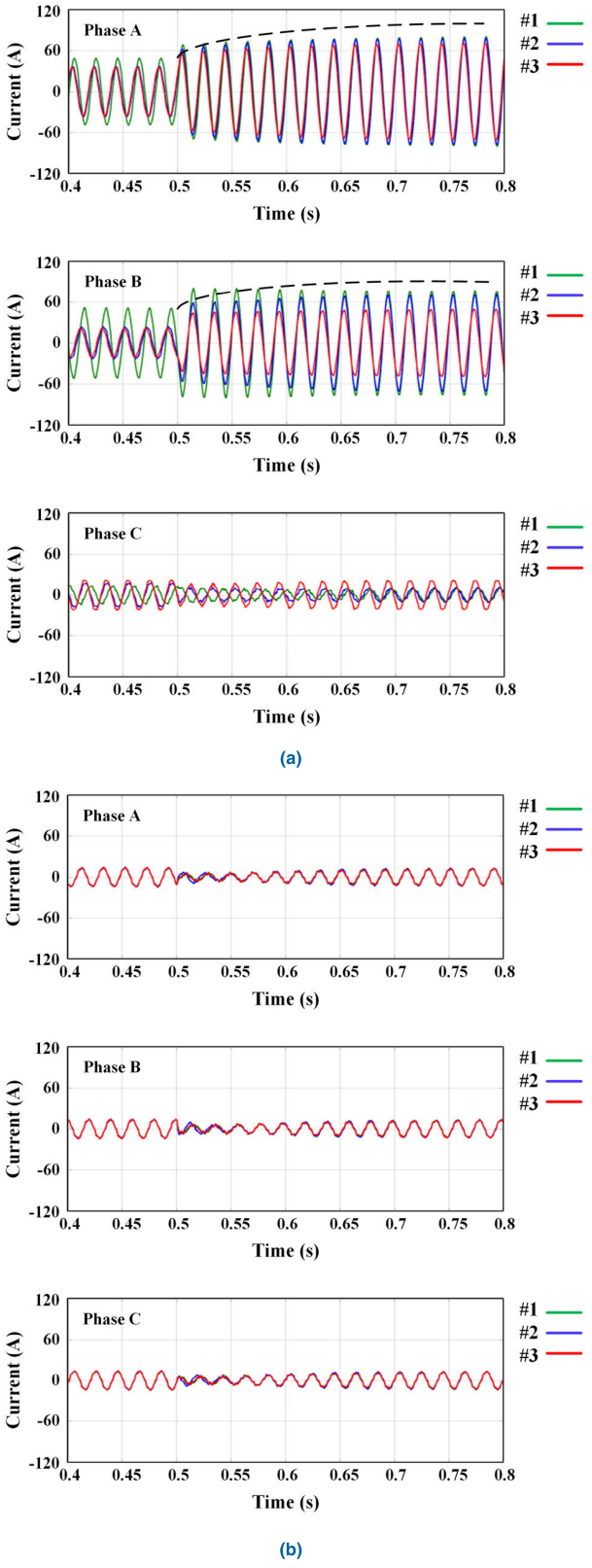

FIGURE 15. Simulated currents obtained in Case 2 with the traditional strategy. (a) 3-phase currents of the three BAT-PCSs. (b) 3-phase currents of the three UC-PCSs.

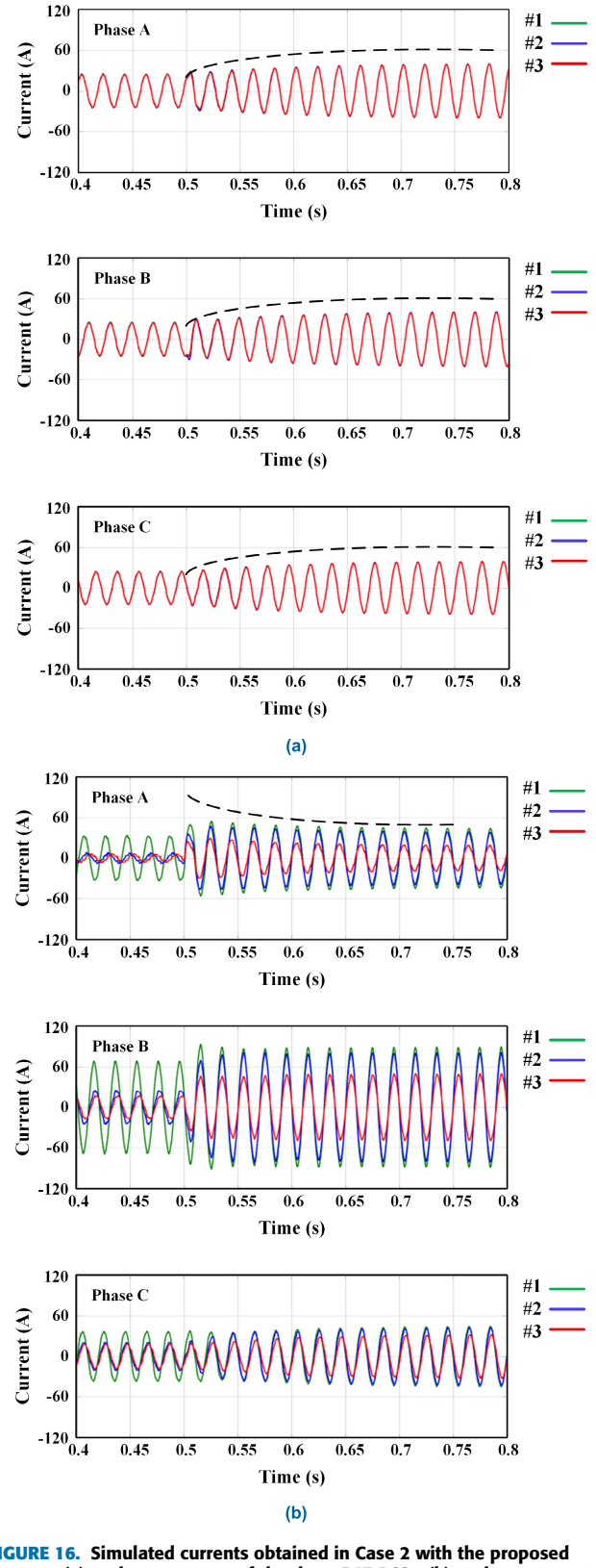

FIGURE 16. Simulated currents obtained in Case 2 with the proposed strategy. (a) 3-phase currents of the three BAT-PCSs. (b) 3-phase currents of the three UC-PCSs.

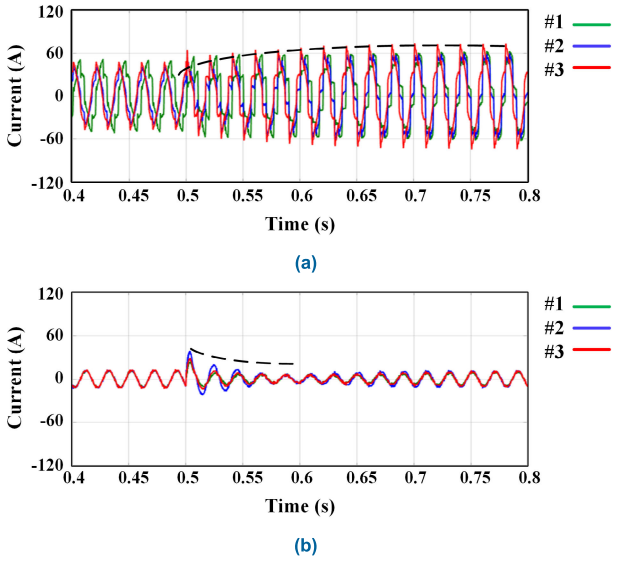

FIGURE 17. Simulated currents obtained in Case 3 with the traditional strategy. (a) Phase A currents of the three BAT-PCSs. (b) Phase A currents of the three UC-PCSs.

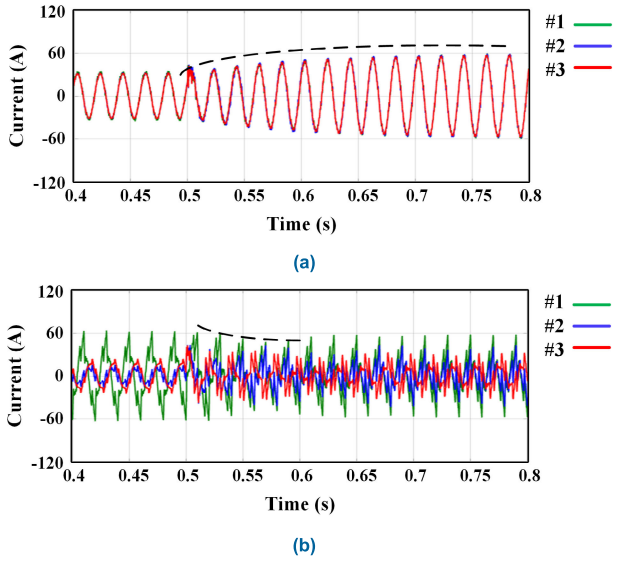

FIGURE 18. Simulated currents obtained in Case 3 with the proposed strategy. (a) Phase A currents of the three BAT-PCSs. (b) Phase A currents of the three UC-PCSs.

inverters 2 and 4 which imitate the operation of the UC-PCS apply the control strategy shown in Figure 7. The structure of the test microgrid is also illustrated in Figure 11. The corresponding inverter parameters are listed in Table 4.

A. CASE 1: BALANCED LOAD

In this experimental case, a 3-phase balanced linear load is connected to the test system. The currents of the inverters 1 and 3 using the conventional droop control method are shown in Figure 20. Due to the different feeder impedances, the two inverters output different currents at the beginning. From the

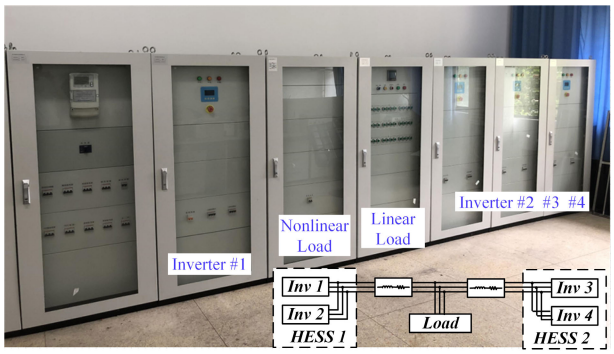

FIGURE 19. Structure of the experimental microgrid.

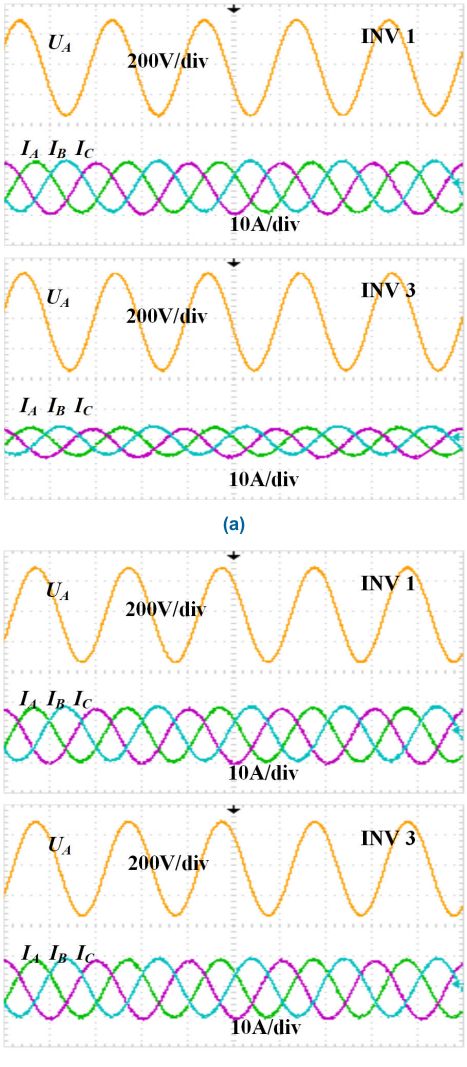

FIGURE 20. Experimental results obtained in Case 1. (a) 3-phase currents and phase A voltage of inverters 1 and 3 before the compensation. (b) 3-phase currents and phase A voltage of inverters 1 and 3 after the compensation.

comparison of the voltage, it can be seen that the currents contain reactive components. When inverter 2 and 4 start the compensation, the currents of inverter 1 and 3 become equal

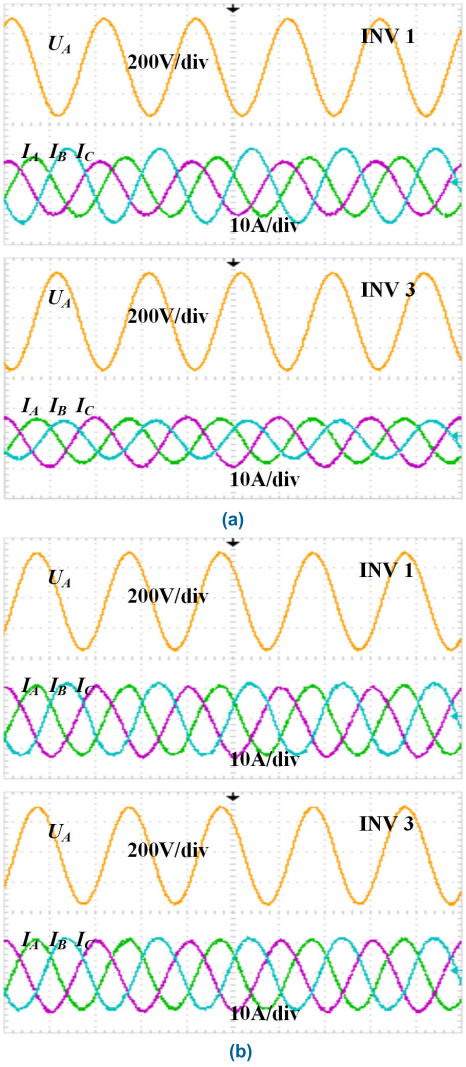

FIGURE 21. Experimental results obtained in Case 2. (a) 3-phase currents and phase A voltage of inverters 1 and 3 before the compensation. (b) 3-phase currents and phase A voltage of inverters 1 and 3 after the compensation.

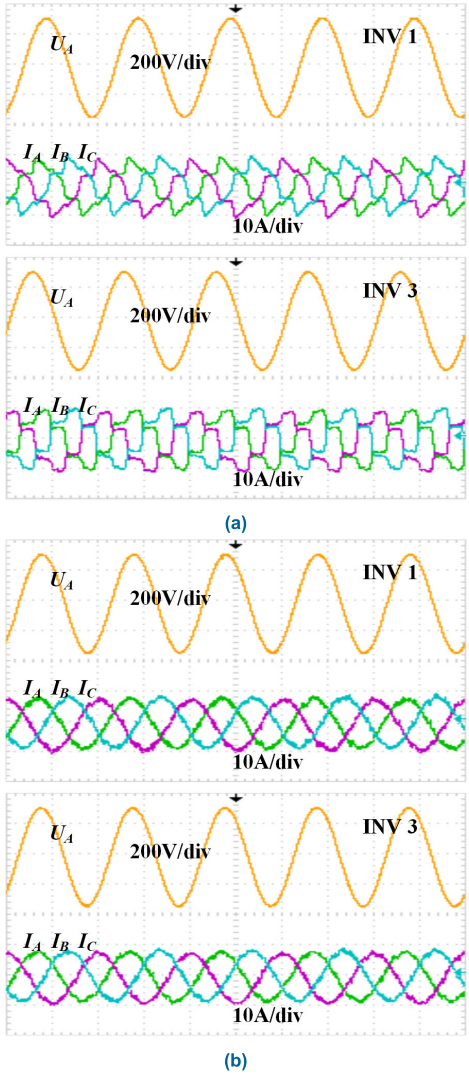

FIGURE 22. Experimental results obtained in Case 3. (a) 3-phase currents and phase A voltage of inverters 1 and 3 before the compensation. (b) 3-phase currents and phase A voltage of inverters 1 and 3 after the compensation.

and only contain active components as shown in Figure 20(b). By maintaining the output current of each battery PCS equal, the power sharing issue is solved.

B. CASE 2: UNBALANCED LOAD

By floating phase C of the load in Case 1, an unbalanced load is obtained. Figure 21(a) illustrates the currents of the inverters 1 and 3 before the compensation. As the test load is unbalanced, there are significant negative sequence currents in the system. After the proposed compensation strategy starts, the output currents of inverters 1 and 3 which imitate the BAT-PCS become symmetrical and equal as shown in Figure 21(b). As inverters 2 and 4 undertake the negative sequence currents and reactive currents, the two inverters 1 and 3 only need to output fundamental active currents. Due to the active power and frequency droop control, these currents are equal.

C. CASE 3: NONLINEAR LOAD

Finally, the proposed coordination control strategy is tested in nonlinear load condition. The performance of the system with the conventional method is shown in Figure 22(a). There are many harmonic components in the currents of inverters 1 and 3. Then, the compensation strategy is started in inverters 2 and 4, making the two inverters work as the APF. As the harmonic currents and reactive currents are absorbed, only the active currents are left in inverters 1 and 3 as shown in Figure 22(b). Finally, the currents of the simulated BAT-PCSs have the same magnitude and phase.

From the above experimental results, it can be seen that the proposed coordination strategy well maintains the output of BAT-PCSs equal and sinusoidal through the compensation role provided by the UC-PCS. Thus, the power sharing among the BAT-PCSs can be realized.

TABLE 4. Different networking strategies of the HESS.

Circuit Parameters		Values
Feeder Line	Feeder 1	$R_{f1} = 0.05\ \Omega$
	Feeder 2	$R_{f2} = 0.10\ \Omega$
Inverter	LC Filter	$L_f = 0.7$ mH, $C_f = 50\ \mu$F
	Frequency	$f_s = 10$ kHz
Control Parameters		**Values**
Inv 1, 3	Droop Slopes	$D_p = 5 \times 10^{-6}$, $D_q = 5 \times 10^{-5}$
	Initial Voltage	$E_0 = 315$ V, $F_0 = 50.15$ Hz
	Voltage Controller	$k_{PV} = 7.6$, $k_{IV} = 76$
	Current Controller	$k_{PI} = 0.2$, $k_{II} = 15$
Inv 2, 4	Current Controller	$k_{PI} = 0.7$

VII. CONCLUSIONS

In this paper, a coordination control strategy is proposed for the HESS composed of BAT-PCS and UC-PCS. Comparing with the traditional strategy, the proposal further studies the power allocation issue under unbalanced and nonlinear load conditions. The strategy mainly has two advantages. Firstly, the static and dynamic performance of the system is enhanced due to the reactive, negative sequence and harmonic power compensation role of the UC-PCS. Secondly, accurate power sharing among BAT-PCSs is realized in networked microgrids; and communication is only used inside HESS. Moreover, the dual inverter structure of HESS is conducive for the upgrading of existing equipment. Simulation and experimental results have verified the effectiveness of the proposed coordination strategy. In the simulation, both the static and dynamic system performances are presented. Due to the compensation role of the UC-PCS, the BAT-PCS only need output low-frequency active power, even in unbalanced or nonlinear load conditions. When several HESSs operate together, each BAT-PCS has the same power output.

However, the strategy only solves the power sharing issue for the BAT-PCSs, the circulating currents still exist among HESSs, which may cause unnecessary line loss. In the future, the power sharing issue of the HESS will be studied to improve the proposed control strategy; meanwhile, economic operation will be considered to make the BAT-PCS output more flexible.

REFERENCES

[1] M. A. Zamani, T. S. Sidhu, and A. Yazdani, "Investigations into the control and protection of an existing distribution network to operate as a microgrid: A case study," *IEEE Trans. Power Electron.*, vol. 61, no. 4, pp. 1904–1915, Apr. 2014.

[2] I.-Y. Chung, W. Liu, D. A. Cartes, E. G. Collins, and S.-I. Moon, "Control methods of inverter-interfaced distributed generators in a microgrid system," *IEEE Trans. Ind. Appl.*, vol. 46, no. 3, pp. 1078–1088, May/Jun. 2010.

[3] Y. Xu, W. Zhang, G. Hug, S. Kar, and Z. Li, "Cooperative control of distributed energy storage systems in a microgrid," *IEEE Trans. Smart Grid*, vol. 6, no. 1, pp. 238–248, Jan. 2015.

[4] M.-E. Choi, S.-W. Kim, and S.-W. Seo, "Energy management optimization in a battery/supercapacitor hybrid energy storage system," *IEEE Trans. Smart Grid*, vol. 3, no. 1, pp. 463–472, Mar. 2012.

[5] M. G. Molina and P. E. Mercado, "Power flow stabilization and control of microgrid with wind generation by superconducting magnetic energy storage," *IEEE Trans. Power Electron.*, vol. 26, no. 6, pp. 910–922, Mar. 2011.

[6] U. Akram, M. Khalid, and S. Shafiq, "An innovative hybrid wind-solar and battery-supercapacitor microgrid system—Development and optimization," *IEEE Access*, vol. 5, pp. 25897–25912, 2017.

[7] A. V. Savkin, M. Khalid, and V. G. Agelidis, "A constrained monotonic charging/discharging strategy for optimal capacity of battery energy storage supporting wind farms," *IEEE Trans. Sustain. Energy*, vol. 7, no. 3, pp. 1224–1231, Jan. 2016.

[8] M. Khalid, A. Ahmadi, A. V. Savkin, and V. G. Agelidis, "Minimizing the energy cost for microgrids integrated with renewable energy resources and conventional generation using controlled battery energy storage," *Renew. Energy*, vol. 97, pp. 646–655, Nov. 2016.

[9] W. Ma, W. Wang, X. Wu, R. Hu, F. Tang, W. Zhang, X. Han, and L. Ding, "Optimal allocation of hybrid energy storage systems for smoothing photovoltaic power fluctuations considering the active power curtailment of photovoltaic," *IEEE Access*, vol. 7, pp. 74787–74799, 2019.

[10] U. Manandhar, N. R. Tummuru, S. K. Kollimalla, A. Ukil, G. H. Beng, and K. Chaudhari, "Validation of faster joint control strategy for battery- and supercapacitor-based energy storage system," *IEEE Trans. Ind. Electron.*, vol. 65, no. 4, pp. 3286–3295, Apr. 2018.

[11] S. K. Kollimalla, M. K. Mishra, A. Ukil, and H. B. Gooi, "DC grid voltage regulation using new HESS control strategy," *IEEE Trans. Sustain. Energy*, vol. 8, no. 2, pp. 772–781, Apr. 2017.

[12] A. Tani, M. B. Camara, and B. Dakyo, "Energy management in the decentralized generation systems based on renewable energy—Ultracapacitors and battery to compensate the wind/load power fluctuations," *IEEE Trans. Ind. Appl.*, vol. 51, no. 2, pp. 1817–1827, Mar./Apr. 2015.

[13] S. Kotra and M. K. Mishra, "A supervisory power management system for a hybrid microgrid with HESS," *IEEE Trans. Ind. Electron.*, vol. 64, no. 5, pp. 3640–3649, May 2017.

[14] R. K. Sharma and S. Mishra, "Dynamic power management and control of a PV PEM fuel-cell-based standalone AC/DC microgrid using hybrid energy storage," *IEEE Trans. Ind. Appl.*, vol. 54, no. 1, pp. 526–538, Jan./Feb. 2018.

[15] S. Mishra and R. K. Sharma, "Dynamic power management of PV based islanded microgrid using hybrid energy storage," in *Proc. 6th IEEE Int. Conf. Power Syst.*, New Delhi, India, Mar. 2016, pp. 1–6.

[16] H. Yin, W. Zhou, M. Li, C. Ma, and C. Zhao, "An adaptive fuzzy logic-based energy management strategy on battery/ultracapacitor hybrid electric vehicles," *IEEE Trans. Transport. Electrific.*, vol. 2, no. 3, pp. 300–311, Sep. 2016.

[17] X. Feng, H. B. Gooi, and S. X. Chen, "Hybrid energy storage with multimode fuzzy power allocator for PV systems," *IEEE Trans. Sustain. Energy*, vol. 5, no. 2, pp. 389–397, Apr. 2014.

[18] B. Hredzak, V. G. Agelidis, and M. Jang, "A model predictive control system for a hybrid battery-ultracapacitor power source," *IEEE Trans. Power Electron.*, vol. 29, no. 3, pp. 1469–1479, Mar. 2014.

[19] D. B. W. Abeywardana, B. Hredzak, and V. G. Agelidis, "A fixed-frequency sliding mode controller for a boost-inverter-based battery-supercapacitor hybrid energy storage system," *IEEE Trans. Power Electron.*, vol. 32, no. 1, pp. 668–680, Jan. 2017.

[20] B. Wang, J. Xu, R.-J. Wai, and B. Cao, "Adaptive sliding-mode with hysteresis control strategy for simple multimode hybrid energy storage system in electric vehicles," *IEEE Trans. Ind. Electron.*, vol. 64, no. 2, pp. 1404–1414, Oct. 2017.

[21] C. N. Rowe, T. J. Summers, R. E. Betz, D. J. Cornforth, and T. G. Moore, "Arctan power–frequency droop for improved microgrid stability," *IEEE Trans. Power Electron.*, vol. 28, no. 8, pp. 3747–3759, Aug. 2013.

[22] I. U. Nutkani, P. C. Loh, and F. Blaabjerg, "Droop scheme with consideration of operating costs," *IEEE Trans. Power Electron.*, vol. 29, no. 3, pp. 1047–1052, Mar. 2014.

[23] Y. Han, H. Li, P. Shen, E. A. A. Coelho, and J. M. Guerrero, "Review of active and reactive power sharing strategies in hierarchical controlled microgrids," *IEEE Trans. Power Electron.*, vol. 32, no. 3, pp. 2427–2451, Mar. 2017.

[24] J. M. Guerrero, L. G. de Vicuna, J. Matas, M. Castilla, and J. Miret, "Output impedance design of parallel-connected UPS inverters with wireless load-sharing control," *IEEE Trans. Ind. Electron.*, vol. 52, no. 4, pp. 1126–1135, Aug. 2005.

[25] Y. Guan, J. M. Guerrero, X. Zhao, J. C. Vasquez, and X. Guo, "A new way of controlling parallel-connected inverters by using synchronous-reference-frame virtual impedance loop—Part I: Control principle," *IEEE Trans. Power Electron.*, vol. 31, no. 6, pp. 4576–4593, Jun. 2016.
[26] J. M. Guerrero, J. C. Vasquez, J. Matas, L. G. de Vicuna, and M. Castilla, "Hierarchical control of droop-controlled AC and DC microgrids—A general approach toward standardization," *IEEE Trans. Ind. Electron.*, vol. 58, no. 1, pp. 158–172, Jan. 2011.
[27] J. M. Guerrero, M. Chandorkar, T.-L. Lee, and P. C. Loh, "Advanced control architectures for intelligent microgrids—Part I: Decentralized and hierarchical control," *IEEE Trans. Ind. Electron.*, vol. 60, no. 4, pp. 1254–1262, Apr. 2013.
[28] Y. Gu, W. Li, and X. He, "Frequency-coordinating virtual impedance for autonomous power management of dc microgrid," *IEEE Trans. Power Electron.*, vol. 30, no. 4, pp. 2328–2337, Apr. 2015.
[29] Q. Xu, X. Hu, P. Wang, J. Xiao, P. Tu, C. Wen, and M. Y. Lee, "A decentralized dynamic power sharing strategy for hybrid energy storage system in autonomous DC microgrid," *IEEE Trans. Ind. Electron.*, vol. 64, no. 7, pp. 5930–5941, Jul. 2017.
[30] Q. Xu, J. Xiao, X. Hu, P. Wang, and M. Y. Lee, "A decentralized power management strategy for hybrid energy storage system with autonomous bus voltage restoration and state-of-charge recovery," *IEEE Trans. Ind. Electron.*, vol. 64, no. 9, pp. 7098–7108, Sep. 2017.
[31] Y. Zhang and Y. W. Li, "Energy management strategy for supercapacitor in droop-controlled DC microgrid using virtual impedance," *IEEE Trans. Power Electron.*, vol. 32, no. 4, pp. 2704–2716, Apr. 2017.
[32] S. Wen, S. Wang, G. Liu, and R. Liu, "Energy management and coordinated control strategy of PV/HESS AC microgrid during Islanded operation," *IEEE Access*, vol. 7, pp. 4432–4441, 2019.
[33] Y. Zhu, F. Zhuo, F. Wang, B. Liu, R. Gou, and Y. Zhao, "A virtual impedance optimization method for reactive power sharing in networked microgrid," *IEEE Trans. Power Electron.*, vol. 31, no. 4, pp. 2890–2904, Apr. 2016.
[34] J. Kim, J. M. Guerrero, P. Rodriguez, R. Teodorescu, and K. Nam, "Mode adaptive droop control with virtual output impedances for an inverter-based flexible AC microgrid," *IEEE Trans. Power Electron.*, vol. 26, no. 3, pp. 689–701, Mar. 2011.
[35] Y. Zhu, F. Zhuo, F. Wang, B. Liu, and Y. Zhao, "A wireless load sharing strategy for islanded microgrid based on feeder current sensing," *IEEE Trans. Power Electron.*, vol. 30, no. 12, pp. 6706–6719, Dec. 2015.
[36] W. Yao, M. Chen, J. Matas, J. M. Guerrero, and Z.-M. Qian, "Design and analysis of the droop control method for parallel inverters considering the impact of the complex impedance on the power sharing," *IEEE Trans. Ind. Electron.*, vol. 58, no. 2, pp. 576–588, Feb. 2011.
[37] J. He and Y. W. Li, "An enhanced microgrid load demand sharing strategy," *IEEE Trans. Power Electron.*, vol. 27, no. 9, pp. 3984–3995, Sep. 2012.
[38] M. Savaghebi, A. Jalilian, J. C. Vasquez, and J. M. Guerrero, "Secondary control scheme for voltage unbalance compensation in an islanded droop-controlled microgrid," *IEEE Trans. Smart Grid*, vol. 3, no. 2, pp. 797–807, Jun. 2012.
[39] Y. Zhang and H. Ma, "Analysis of networked control schemes and data-processing method for parallel inverters," *IEEE Trans. Ind. Electron.*, vol. 61, no. 4, pp. 1834–1844, Apr. 2014.
[40] H. Zhang, S. Kim, Q. Sun, and J. Zhou, "Distributed adaptive virtual impedance control for accurate reactive power sharing based on consensus control in microgrids," *IEEE Trans. Smart Grid*, vol. 8, no. 4, pp. 1749–1761, Jul. 2017.
[41] F. Guo, C. Wen, J. Mao, and Y.-D. Song, "Distributed secondary voltage and frequency restoration control of droop-controlled inverter-based microgrids," *IEEE Trans. Ind. Electron.*, vol. 62, no. 7, pp. 4355–4364, Jul. 2015.
[42] Y. Zhu, Q. Fan, B. Liu, and T. Wang, "An enhanced virtual impedance optimization method for reactive power sharing in microgrids," *IEEE Trans. Power Electron.*, vol. 33, no. 12, pp. 10390–10402, Dec. 2018.
[43] J. He, Y. W. Li, J. M. Guerrero, F. Blaabjerg, and J. C. Vasquez, "An islanding microgrid power sharing approach using enhanced virtual impedance control scheme," *IEEE Trans. Power Electron.*, vol. 28, no. 11, pp. 5272–5282, Nov. 2013.
[44] J. He, Y. W. Li, and F. Blaabjerg, "An enhanced islanding microgrid reactive power, imbalance power, and harmonic power sharing scheme," *IEEE Trans. Power Electron.*, vol. 30, no. 6, pp. 3389–3401, Jun. 2015.
[45] J. Zhou, S. Kim, H. Zhang, Q. Sun, and R. Han, "Consensus-based distributed control for accurate reactive, harmonic, and imbalance power sharing in microgrids," *IEEE Trans. Smart Grid*, vol. 9, no. 4, pp. 2453–2467, Jul. 2018.
[46] P. Rodriguez, A. Luna, I. Candela, R. Mujal, R. Teodorescu, and F. Blaabjerg, "Multiresonant frequency-locked loop for grid synchronization of power converters under distorted grid conditions," *IEEE Trans. Ind. Electron.*, vol. 58, no. 1, pp. 127–138, Jan. 2011.

YIXIN ZHU (S'11–M'17) received the B.S., M.S., and Ph.D. degrees in electrical engineering from Xi'an Jiaotong University, Xi'an, China, in 2009, 2011, and 2015, respectively. In 2016, he joined Jiangnan University as a Lecturer, where he is currently with the School of the IoT Engineering. His research interests include the design, control, and application of the high-power active power filter, the photovoltaic grid-connected inverter, and the modeling, analysis, and power management of the microgrid.

QIGAO FAN (M'18) received the B.S. and M.S. degrees in control and instrumentation, and the Ph.D. degree in mechatronic engineering from the China University of Mining Technology, China, in 2008, 2010, and 2013, respectively. In 2013, he joined Jiangnan University as a Lecturer, where he is currently an Associate Professor of electrical engineering with the School of the IoT Engineering. His research interests include indoor localization, robotics, intelligent casting, wireless MEMS-based technologies, and the IoT sensor technology.

LIANSONG XIONG (S'12–M'16) was born in Sichuan, China, in 1986. He received the B.S., M.S., and Ph.D. degrees in electrical engineering from Xi'an Jiaotong University (XJTU), in 2009, 2012, and 2016, respectively. In June 2016, he joined the Nanjing Institute of Technology (NJIT), introduced in High-Level Academic Talent Plan of NJIT. Since November 2017, he has been with the Department of Electrical Engineering, Hong Kong Polytechnic University, as a Research Associate. His research interests include power quality, multilevel converter, renewable energy, stability analysis, etc.

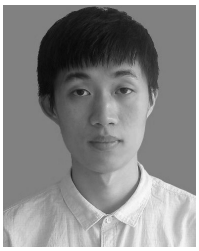

GAOFENG ZHANG received the B.S. degree from Wuhan Textile University, China, in 2017. He is currently pursuing the M.S. degree in electrical engineering with Jiangnan University. His main research interests include microgrid and electric vehicle.

XIN QIAN received the B.S. degree from the Huaiyin Institute of Technology, China, in 2018. He is currently pursuing the M.S. degree in electrical engineering with Jiangnan University. His main research interests include microgrid and renewable energy power generation.